RESIDUAL STRENGTH PREDICTION OF FUSELAGE STRUCTURES WITH MULTIPLE SITE DAMAGE

Chuin-Shan Chen, Paul A. Wawrzynek, and Anthony R. Ingraffea

The Cornell University Fracture Group
641 Rhodes Hall, Cornell University
Ithaca, New York, 14853, USA

(607) 254-8815
www.cfg.cornell.edu

ABSTRACT

This paper summarizes recent results on simulating full-scale pressure tests of wide body, lap-jointed fuselage panels with multiple site damage (MSD). The crack tip opening angle (CTOA) fracture criterion and the FRANC3D/STAGS software program were used to analyze stable crack growth under conditions of general yielding. The link-up of multiple cracks and residual strength of damaged structures were predicted. Elastic-plastic finite element analysis based on the von Mises yield criterion and incremental flow theory with small strain assumption was used. A global-local modeling procedure was employed in the numerical analyses.

Stress distributions from the numerical simulations are compared with strain gage measurements. Analysis results show that accurate representation of the load transfer through the rivets is crucial for the model to predict the stress distribution accurately. Predicted crack growth and residual strength are compared with test data. Observed and predicted results both indicate that the occurrence of small MSD cracks substantially reduces the residual strength. Modeling fatigue closure is essential to capture the fracture behavior during the early stable crack growth. Breakage of a tear strap can have a major influence on residual strength prediction.

1 INTRODUCTION

Modern aircraft structures are designed using a damage tolerance philosophy. This design philosophy envisions sufficient strength and structural integrity of the aircraft to sustain major damage and to avoid catastrophic failure. However, structural aging of the aircraft may significantly reduce the residual strength, which raises many important safety issues.

One of the most notable problems in aging aircraft is widespread fatigue damage (WFD). WFD has two subsets, multiple site damage (MSD) and multiple element damage (MED). This paper presents recent results on simulating full-scale pressure tests of wide body, lap-jointed fuselage panels with MSD [1, 2]. The tests, funded by the Federal Aviation Administration (FAA), and performed by the Boeing Commercial Airplane Group, were intended to characterize crack growth in a generic wide body, lap-jointed fuselage configuration subjected to MSD. The FRANC3D/STAGS program [3, 4, 5, 6] was used to perform the numerical analyses. The

crack tip opening angle (CTOA) fracture criterion [7, 8, 9] was used to control stable crack advancement. Calculated stress distributions are compared with strain gage readings. Predicted crack growth and residual strength results are then compared with experimental measurements.

2 FULL-SCALE FUSELAGE PANEL TESTING

The full-scale fuselage panel tests investigated in this study were performed on a wide body pressure test fixture with a radius of curvature of 127 inches. A brief overview of the panel tests is presented below. More information about the fixtures and tests can be found in [10, 11, 1, 2].

Two identical curved lap-jointed panels were fabricated. The test panels were designed to simulate typical wide body fuselage crown structures consisting of bonded tear straps and floating frames connected to hat section stringers with stringer clips. Skins and tear straps were made of 0.063 inch thick, 2024-T3 clad aluminum alloy. Stringers, frames, and stringer clips were made of 7075-T6 aluminum clad. The skins were joined by the lap joints. The joint was a typical three row configuration assembled using standard 3/16 inch diameter, 100° countersunk-head rivets. The tear straps were hot bonded to the skins at each frame station. The outer and inner tear straps were overlapped above the lap joint. The detailed dimensions of panels, frames, stringers, and stringer clips can be found in [1, 2].

A five-inch initial saw cut was inserted along the upper rivet row in the outer skin. For the panel with MSD cracks, small sawcuts were inserted in the outer skin after the rivet holes had been drilled, but prior to the application of the fay sealant and rivet installation. The panels were subjected to pressure cycling until the length of the crack reached about two frame bays for the residual strength tests. The central frame was then cut prior to static loading to failure. Rosette strain gages were installed back-to-back on the skins and tear straps in the vicinity of the lap joint.

3 NUMERICAL MODEL

All structural components including skins, stringers, and frames were modeled by displacement-based four-noded or five-noded quadrilateral shell elements [12, 13]. Each node of the shell element has six degrees of freedom. To analyze the panel tests with reasonable computer resources and sufficient accuracy, a global-local approach was used. Figure 1 shows the typical finite element meshes for the two hierarchical modeling levels employed in the simulations. A 12-stringer bay wide and 5-frame bay long panel, which is about the size of the test panel, was modeled at the global level. A 1x1 bay stiffened panel was modeled at the local level. The local model differed from the global model in the finite element mesh density and the detailed geometric modeling of the cross sectional shapes of stringers and frames.

Pressure loading was applied on all the external skins. Symmetric boundary conditions were imposed on all the boundary edges of the global model to simulate a cylinder-like fuselage structure. Uniform axial expansion was allowed at one longitudinal end. On this boundary edge, an axial force equal to $(PR/2) \cdot L$ was assigned where P is the applied pressure, R is the radius of the panel, and L is the arc-length of the edge. The kinematic boundary conditions (displacements and rotations) applied along the boundaries of the local model were extracted from the global model results. In addition to these kinematic constraints, the local model was also subjected to internal pressure.

A piecewise linear representation was used for the uniaxial stress-strain curves for 2024-T3

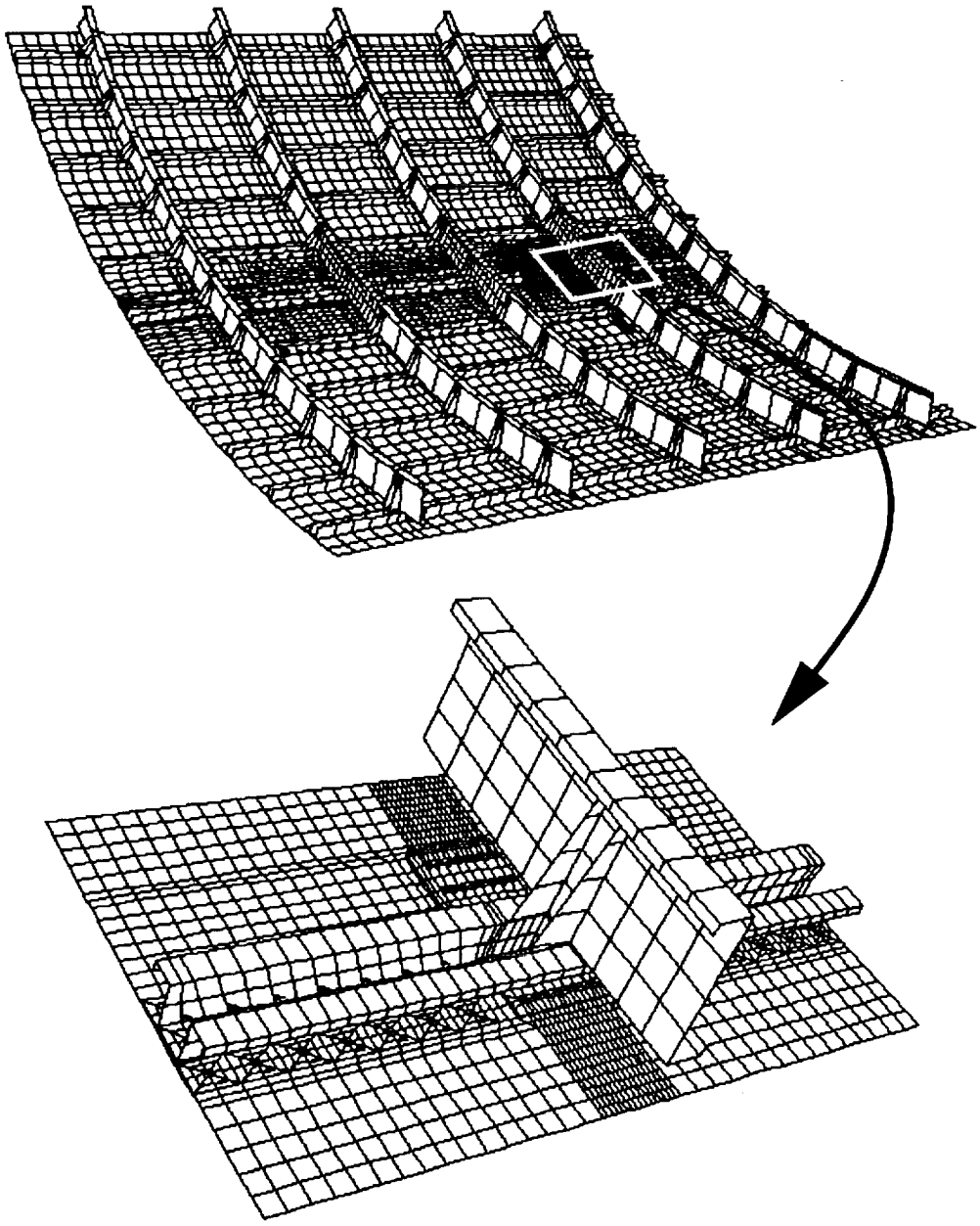

Figure 1: Global and local finite element models.

and 7075-T6 aluminum alloys (see Figures 2 and 3). Rivets were modeled by elastic-plastic spring elements that connect finite element nodes in the upper and lower skins and tear straps. Each rivet was modeled with six degrees of freedom, corresponding to extension, shearing, bending and twisting of the rivet. The stiffness of each degree of freedom was defined by prescribing a piecewise linear force-deflection curve. The axial, flexural, and torsional stiffnesses of the spring element were computed by assuming that the rivet behaves like a simple elastic rod with a diameter of 3/16 inch. The elastic shear stiffness of the rivet was computed by the following empirical relation developed by Swift [14]:

$$K_{rivet} = \frac{ED}{[A + C(D/t_1 + D/t_2)]} \tag{1}$$

where E is the elastic modulus of sheet material, D is the rivet diameter, t_1 and t_2 are thicknesses of joined sheets, and $A = 5.0$ and $C = 0.8$ for aluminum rivets. Initial shear yielding and ultimate shear strength of rivets were assumed to occur at load levels of 600 lb and 1080 lb, respectively. Once a rivet reaches its ultimate strength, it will *break* and lose its load carrying capacity. The force-deflection curve shown in Figure 4 for shearing is intended to represent, empirically, the net shear stiffness of a rivet-joined sheet connection, accounting for bearing deformations and local yielding around the rivet [14, 15].

The adhesive bond between skin and tear strap was also modeled with spring elements. The shear stiffness for the springs was computed based on an *effective* area of the adhesive with [16]:

$$K_{adhesive} = \frac{A_{eff}}{t_a/G_a + (3/8)(t_1/G + t_2/G))} \tag{2}$$

where A_{eff} is the bond area being lumped at the finite element nodal connection, G is the elastic shear modulus of sheet material, G_a is the elastic shear modulus of adhesive, t_1 and t_2 are the thicknesses of bonded sheets, and t_a is the thickness of adhesive bond. Because no adhesive tests were conducted, the material properties of adhesive, G_a and t_a, were obtained from the experimental results in [17]. The maximum shear deflection was assumed to be 0.001 inch. Similar to the rivet spring, once the adhesive spring reaches its ultimate strength, it will *break* and lose its load carrying capacity. The force-deflection curve for shearing is shown in Figure 5. The axial stiffness of the adhesive spring was derived from the shear stiffness. The torsional and flexural stiffnesses of adhesive were assumed to be negligible.

Both geometric and material nonlinearities were used in the analysis at the global and local modeling levels. The global shell model captures the overall nonlinear response of the stiffened, curved, pressurized structure. The local shell model provides the detailed deformation and stress field near the crack tips to compute the fracture parameters (*e.g.*, CTOA) that control crack growth.

4 DETERMINATION OF CTOA$_c$

Flat panel tests were conducted by the Boeing Commercial Airplane Group to obtain material properties for fatigue and fracture analysis of the curved fuselage panels. Four 48 inch wide, 80 inch long, 0.063 inch thick middle crack tension (MT) specimens were tested. The flat panel specimens were made from the same aluminum sheet used for the skin of the curved fuselage panels. A constant amplitude cyclic loading was applied to propagate an initial sawcut. After the fatigue crack growth, a residual strength test was conducted under a monotonically

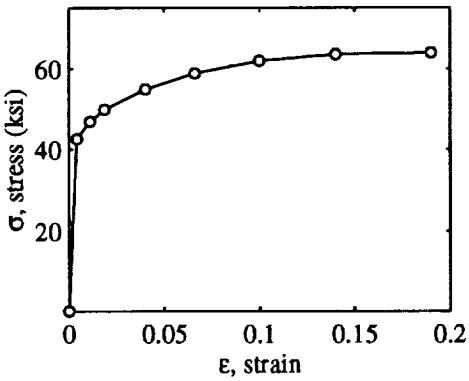

stress (ksi)	strain
0.0	0.0
42.7	0.0040667
47.0	0.011
50.0	0.0186
55.0	0.0399
59.0	0.066
62.0	0.1
63.6	0.14
64.0	0.19

E = 1.05e+04 ksi
ν = 0.33

Figure 2: Piecewise linear representation of the uniaxial stress-strain curve for 2024-T3 aluminum.

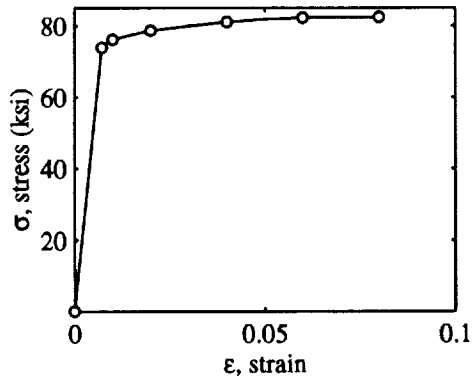

stress (ksi)	strain
0.0	0.0
74.0	0.00718
76.2	0.01
78.7	0.02
81.1	0.04
82.2	0.06
82.4	0.08

E = 1.03e+04 ksi
ν = 0.33

Figure 3: Piecewise linear representation of the uniaxial stress-strain curve for 7075-T6 aluminum.

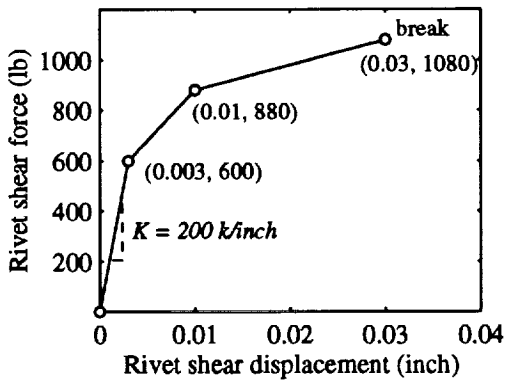

Figure 4: Shear stiffness and strength of rivet spring.

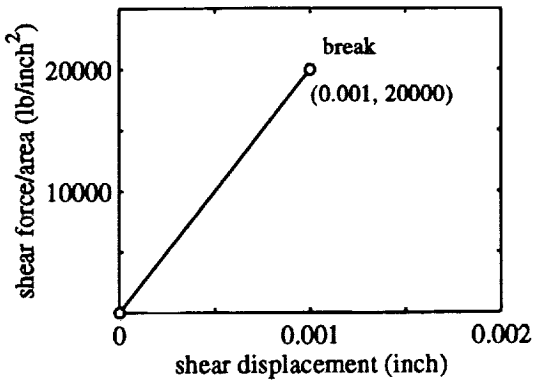

Figure 5: Shear stiffness and strength of adhesive spring.

TABLE 1: TEST MATRIX FOR MT SPECIMENS (AFTER [1])

Specimen ID	half initial crack (inch)	half final fatigue crack (inch)	$\sigma_{fatigue}$ (ksi)	R
2024_FAA_TL3	2.0	8.0	8.0	0.1
2024_FAA_TL4	2.0	5.5	16.0	0.1
	5.5	8.0	8.0	
2024_FAA_TL5	5.0	12.0	12.0	0.1
2024_FAA_TL6	2.0	8.0	7.0	0.5

increasing load. The test matrix prior to the residual strength test is summarized in Table 1. Visual crack extension measurements were taken. Surface $CTOA_c$ was measured for Specimen 2024_FAA_TL3 during the residual strength test. Nine values were obtained and the mean of the measured critical angles was about 5.5 degrees with a scatter band about $\pm 1.0°$.

The value of $CTOA_c$ used in the residual strength analysis of the fuselage panels was determined by finding an angle within the scatter band of the $CTOA_c$ measurements that best correlates with the observed crack growth and residual strength of the coupon tests. The FRANC3D/STAGS program was used to simulate fracture behavior of the MT specimens. A finite element mesh that models a quarter of the specimen with a crack tip element size of 0.04 inch and a half plane strain core height equal to 0.08 inch is shown in Figure 6. A plane strain core is used to capture the three-dimensional (3D) constraint effects developed at the local crack tip [18, 19, 20]. The half core height is about the thickness of the specimen.

Figure 7 compares the predicted crack growth results to the experimental measurements. The $CTOA_c$ of 4.5 degrees best correlates the predicted and measured residual strengths. However, it under-estimates the applied stress at the earlier stage of stable crack growth. The 5 and 5.5 degree critical angles give a better correlation for the earlier crack growth but over-predict the residual strength by 8.5% and 14.3%, respectively.

The discrepancy between predicted and measured crack growth at the earlier stage of tearing might relate to the residual plastic deformation left by the fatigue crack growth. This effectively increases the crack opening resistance during early stable crack growth [21]. The plastic wake

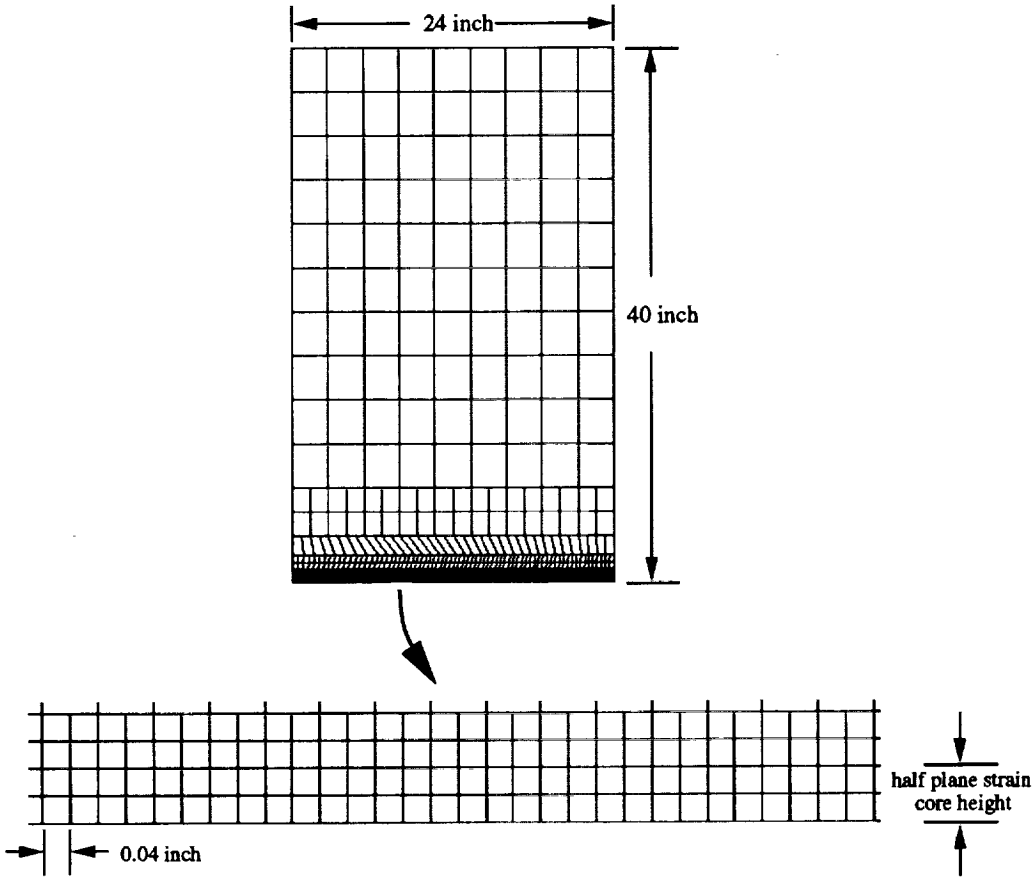

Figure 6: Finite element mesh for one quarter of 48x80 inch MT specimen.

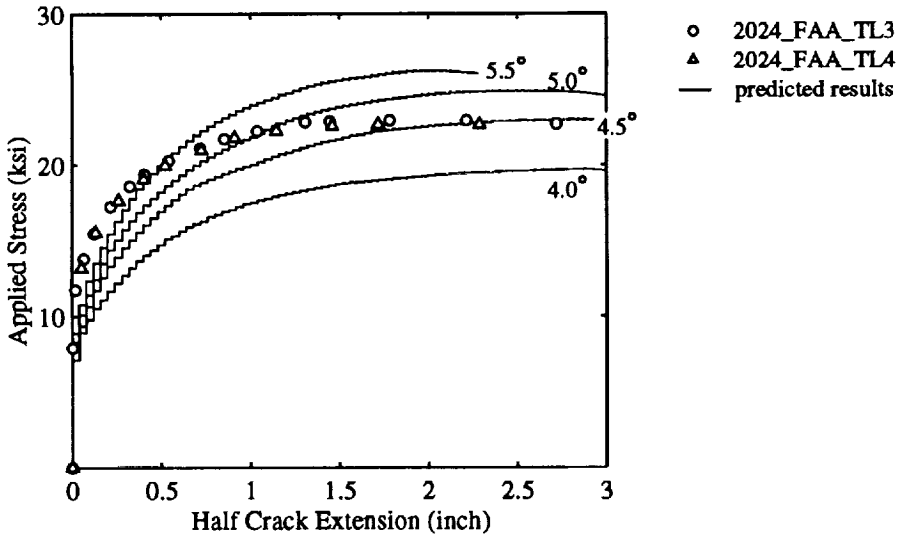

Figure 7: Predicted applied stress versus crack growth for 48 inch wide MT specimen (half plane strain core height = 0.08 inch).

effect on crack growth and residual strength analysis will be further discussed in Section 6.

5 NUMERICAL RESULTS: STRAIN GAGE COMPARISON

Strain gage comparisons were made to verify predicted stress distributions. Figure 8 shows the overall deformed structures for both the global and local models. Convergence studies were conducted to ensure accuracy of deformations and stress distributions. Major results from the studies are summarized below:

- For global models, the predicted results converged quickly. The predicted membrane hoop stresses agree well with experimental measurements. The predicted bending hoop stresses are comparable to experimental measurements as one refines the finite element meshes (Figure 9).

- Predicted results from a local model with about the same mesh density as the corresponding region in the global model agree well with global model predictions and experimental measurements. The agreement ensures the transition accuracy in the hierarchical modeling.

- Results with a much higher mesh density that is suitable for crack growth analysis disagree with the rest of the numerical predictions and experimental measurements. The discrepancy is related to the idealized representation of the two-noded spring element for the rivet connection in the finite element model [15, 22]. The single point connection results in unrealistic distortion of the surrounding shell elements. The local distortion causes premature yielding of the shell elements and reduces the load transfer from sheet to rivet. This artificial distortion of the shell elements is discretization-dependent [22, pp. 318–327]. Refining the mesh captures the local artificial distortion better, but makes the comparison to strain gage readings worse [15].

Two modeling idealizations are proposed to avoid this artificial effect. One is to faithfully represent the geometry of the rivets and their interference with the sheets. This would considerably increase the required computational resources and may not be simple to implement in thin-shell elastic-plastic crack growth analysis. The other approach is to generate distributed connections between the two-noded spring element and the surrounding shell elements [15]. The load distribution can be accomplished by defining rigid links, stiff spring elements, or a least-squares loading condition to connect the rivet-spring node to the surrounding shell-element nodes. Care must be taken while defining the area in the shell elements over which the rivet load is distributed. The area should be of the order of the rivet cross-sectional area, since distributing the load over a larger area may inadvertently stiffen the shell elements.

Figure 10 illustrates simulation of the distributed connection using stiff spring elements. Stiff spring elements with an order of magnitude higher stiffness than the rivet spring element are used to distribute the rivet load. For a rivet located on a prescribed tearing path, it is expected that the rivet stays intact on only one side of the crack as the crack propagates around the rivet. Thus, only the shell elements on this side of the crack are used to model the distributed rivet connection. Figure 11 shows the predicted hoop stress distributions with distributed connection simulations. A much better prediction is observed. The local mesh model with the distributed rivet connection was used for crack growth and residual strength analyses.

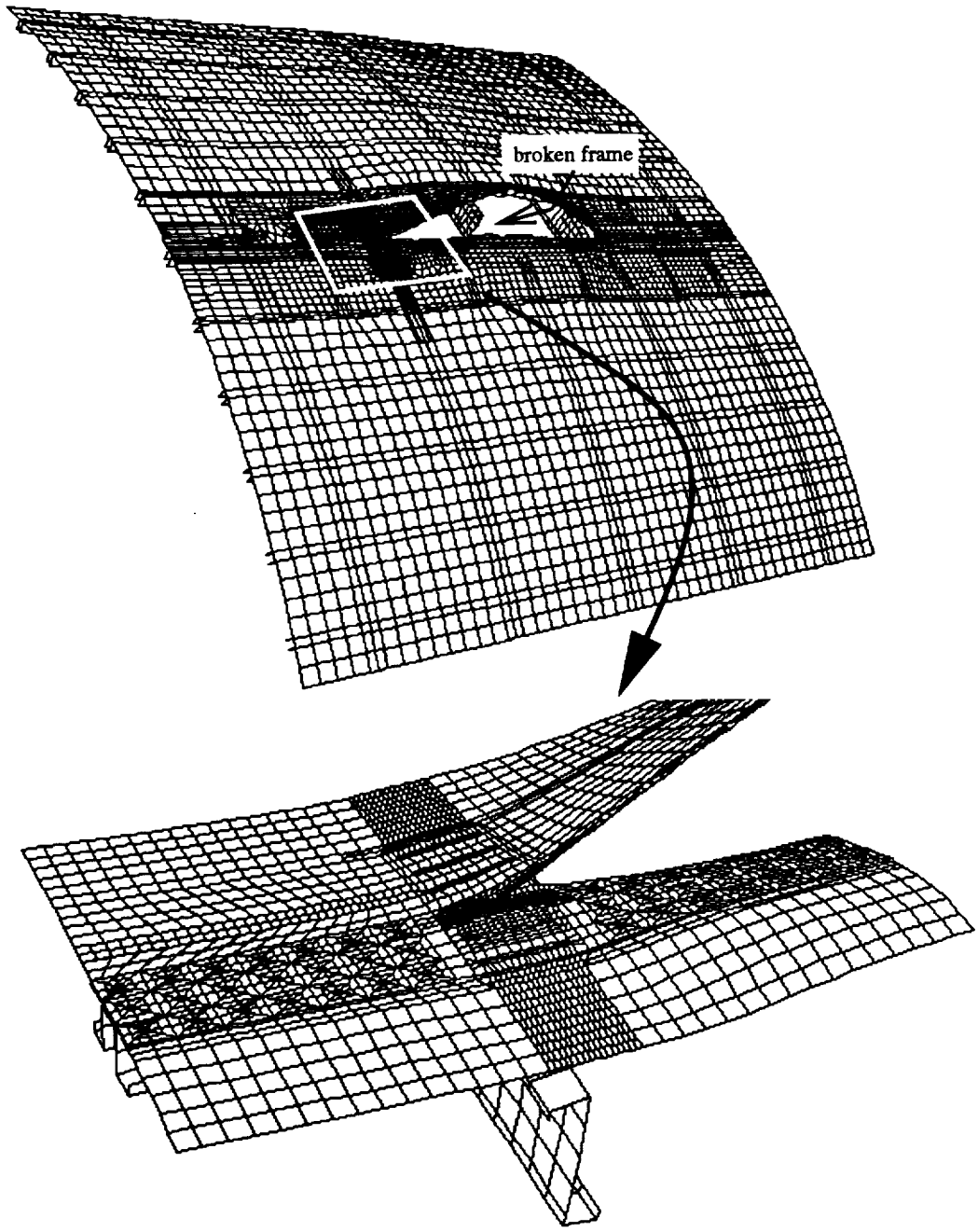

Figure 8: Deformed structures of the validation example at global and local modeling levels (pressure = 9.4 psi, crack length = 38.2 inch, magnification factor = 5.0).

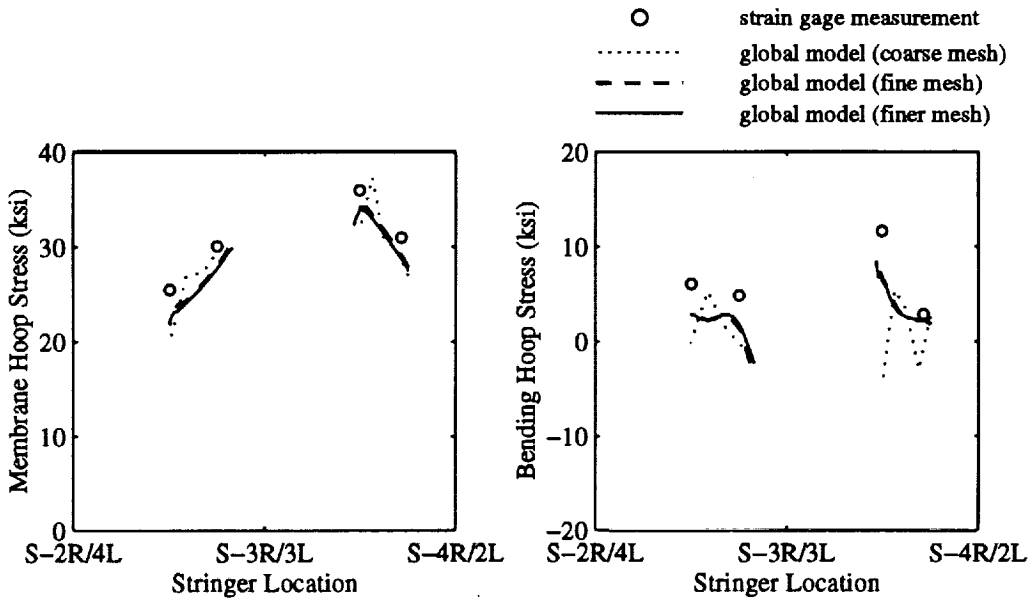

Figure 9: Global convergence study: comparison between computed and measured hoop stresses (pressure = 9.4 psi; crack length = 38.2 in.; frame cut; No MSD).

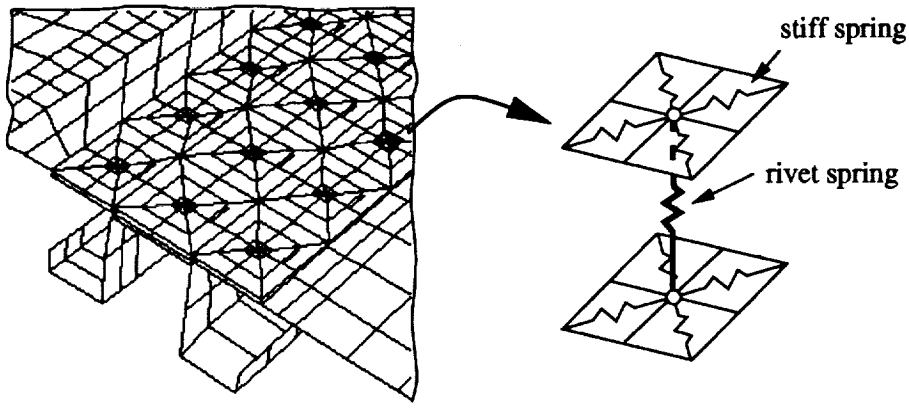

Figure 10: Illustration of distributed connection that connects a fastener node to surrounding shell nodes

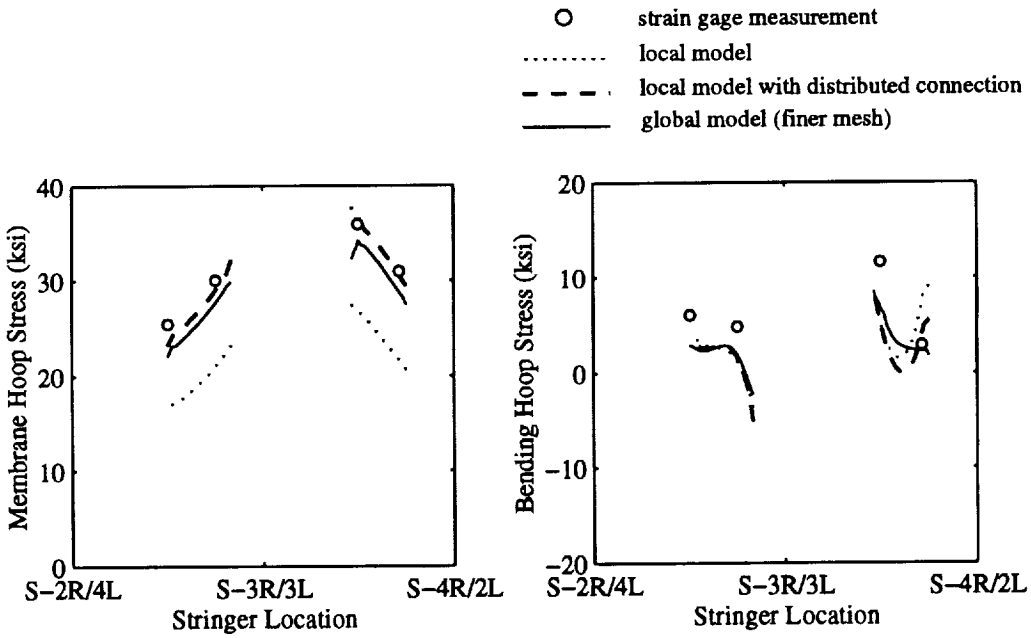

Figure 11: Effects of distributed rivet connection: comparison between computed and measured hoop stresses (pressure = 9.4 psi; crack length = 38.2 in.; frame cut; No MSD).

6 NUMERICAL RESULTS: CRACK GROWTH AND RESIDUAL STRENGTH ANALYSIS

Elastic-plastic crack growth and residual strength analyses were conducted using the local model. Both 4.5 and 5.5 degree critical angles computed at 0.04 inch behind the growing crack tip were used to investigate the sensitivity of $CTOA_c$ on crack growth and residual strength prediction. The 4.5° $CTOA_c$ is the angle that best correlates the predicted and observed residual strengths of the MT tests. The 5.5° angle is the mean from the surface $CTOA_c$ measurements in the MT tests. The plane strain core height was 0.16 inch along the prescribed tearing path.

Figure 12 shows predicted results from the first attempt at crack growth analysis. The change of the $CTOA_c$ from 4.5° to 5.5° increases predicted residual strength by about 33% and 22% for the cases without and with MSD cracks, respectively.

Although analysis results in Figure 12 clearly demonstrate the loss of residual strength due to the presence of MSD, all the predicted results (i) under-estimate the pressure loading to initiate the stable crack growth, and (ii) over-estimate the residual strength.

The much lower predicted pressure for tearing initiation is mainly caused by residual plastic deformation left by the fatigue crack growth. A possible cause for the lower residual strengths observed in the test may be related to the occurrence of tear strap failure. Both effects are discussed below.

6.1 RESIDUAL PLASTIC DEFORMATION EFFECTS

The test panels were subjected to pressure cycling prior to the residual strength test. To incorporate the residual plastic deformations due to the cyclic loading, the residual strength analyses were re-performed using an elastic-plastic cyclic loading simulation suggested by Newman [23].

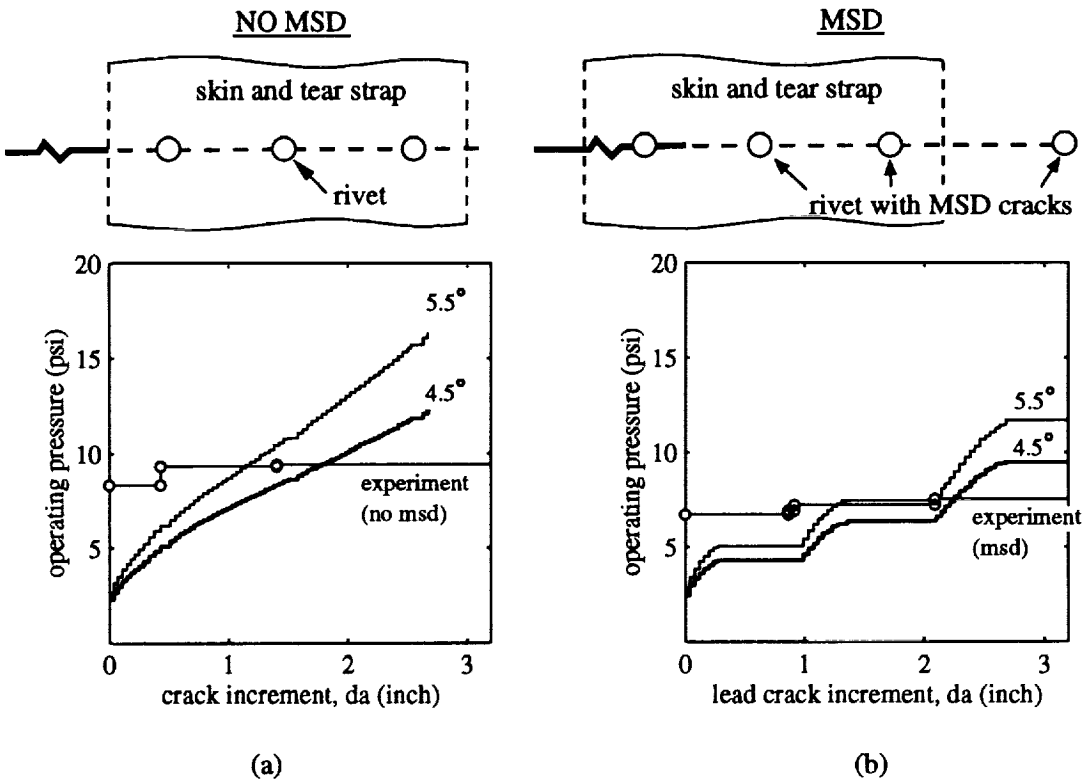

Figure 12: Comparison between the predicted crack growth and experimental measurements: (a) without MSD, and (b) with MSD.

The procedures consist of the following steps:

step 1 *Close* an appropriate length of fatigue crack.

step 2 Load the fuselage model to the maximum pressure loading conducted in fatigue tests.

step 3 Release the crack tip node and unload the model.

step 4 Repeat steps 2 and 3 until the crack tip reaches the initial position for stable tearing.

This procedure implies that the fatigue crack only propagates at the maximum pressure during the cyclic loading simulation. For Mode-I only deformations under constant-amplitude load cycling, crack surfaces close at a positive applied load (*i.e.*, step 3). The contact stresses cause the material to yield in compression. Crack face contact and reverse yielding were not modeled in the current simulations.

In subsequent analyses, the fuselage model is brought to the operating pressure level during fatigue tests without allowing the crack to advance. The crack is then allowed to advance one element, and the load is returned to zero. Figure 13 illustrates results for a 0.32 inch *length* of fatigue closure used in the analysis for the case without MSD cracks. The crack-opening and crack-closure pressures in the fuselage panel simulations follow similar trends observed in the MT flat panel simulations [23]. After two cycles of simulation, the crack-opening and crack-closure pressures quickly stabilize to 7.2 psi and 5.3 psi, respectively.

Figure 14 shows two predicted crack opening profiles when the pressure loading reaches 8.6 psi (no growth), one with fatigue closure effects and the other without. The effects of residual plastic deformations on the crack opening profile and consequently, the CTOA prediction, are clearly observed.

The 7.2 psi crack-opening pressure shown in Figure 13 seems to be too high in comparison with 2D plane stress results [23] and laboratory observations [24, 25]. This may be due to lack of modeling of contact conditions when the crack closes. That is, the crack faces pass each other so no compressive yielding is developed in the unloaded state. The compressive yielding stress will reduce residual tensile plastic deformation thus leading to a lower crack-opening pressure [23].

Figure 15 illustrates results for a 0.08 inch *length* of fatigue crack closure used for the case with MSD cracks. During cyclic loading simulation, the lead and MSD crack tips are released simultaneously. The crack-opening and crack-closure pressures at the second loading cycle for the lead crack are about 4.7 psi and 3.3 psi, respectively. We note that the *length* of fatigue crack closure is restrained by the *length* of MSD cracks. Further amount of fatigue crack closure simulation is possible but leads to somewhat ambiguous MSD fatigue crack propagation. The results after two cycles of simulation, however, is believed to essentially capture the residual plastic deformation effects based on those observed from the case without MSD cracks (Figure 13).

Figure 16 shows predicted crack growth that incorporates the closure effects. Table 2 summarizes the predicted and observed starting pressure to initiate the stable crack growth. The plasticity-induced closure increases the initiation pressure by about 150% to 210%. The predicted crack initiation loads are within 6% of experimental measurements for the cases that incorporate prior plastic residual deformations due to fatigue crack growth. However, the predicted residual strengths are still higher than those observed.

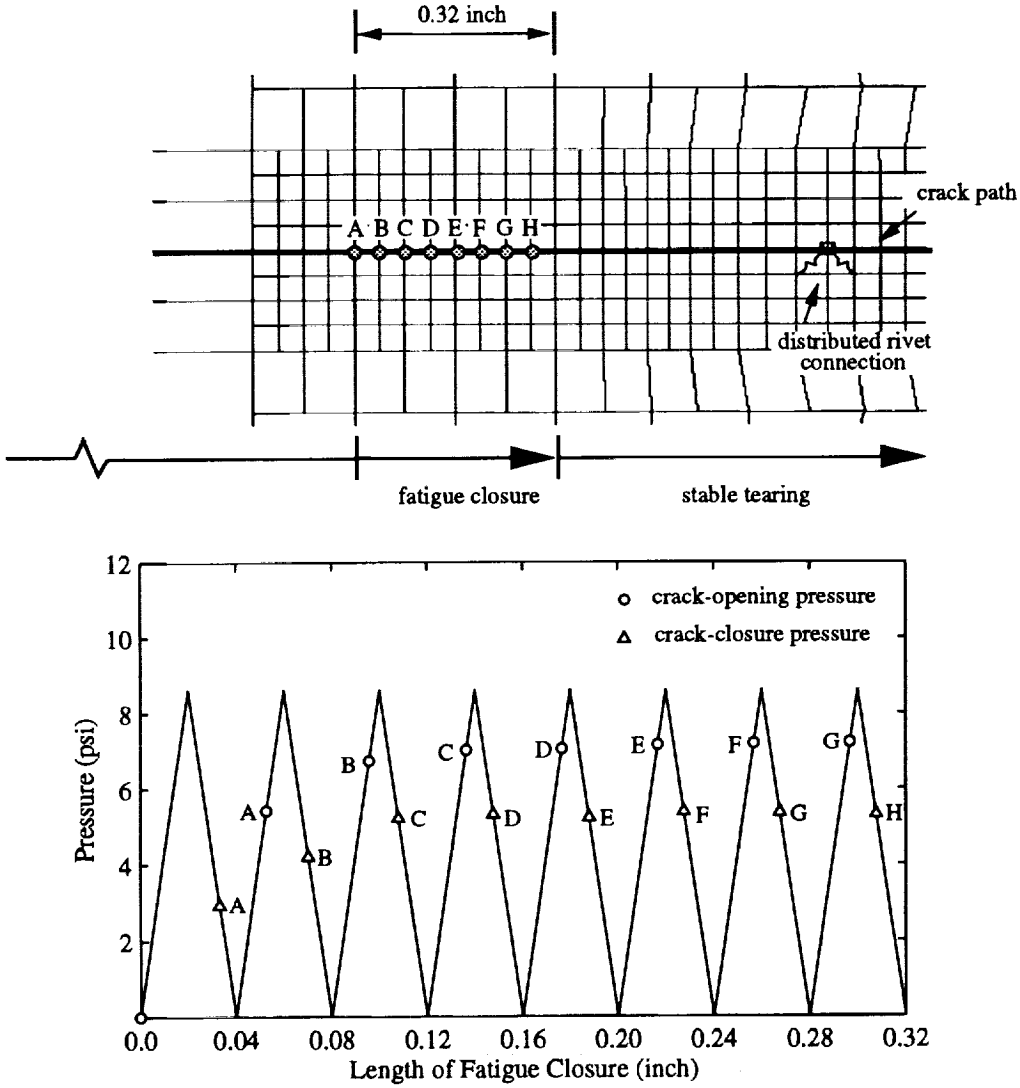

Figure 13: Predicted crack-opening and crack-closure pressure under cyclic loading (cyclic pressure = 8.6 psi, No MSD).

TABLE 2: PREDICTED AND OBSERVED LOADING FOR TEARING INITIATION

	predicted (psi)		observed (psi)
	$CTOA_c = 4.5°$	$CTOA_c = 5.5°$	
No MSD	2.3	2.7	8.3
No MSD (0.32 inch closure)	8.3	8.4	8.3
MSD	2.5	2.8	6.7
MSD (0.08 inch closure)	6.3	6.5	6.7

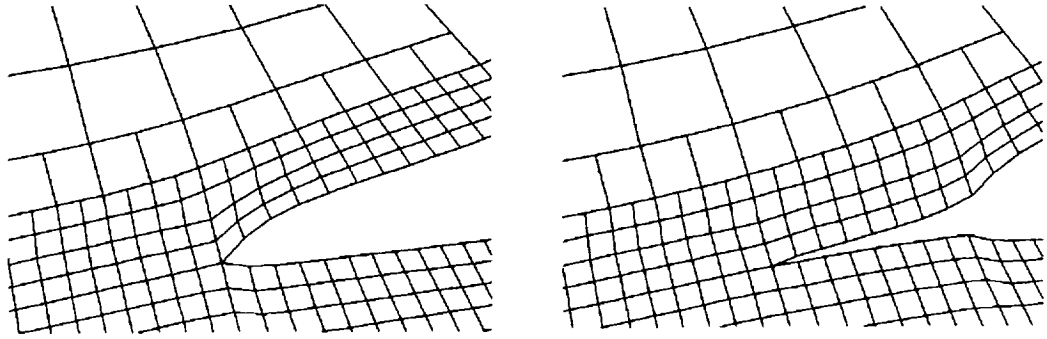

Figure 14: Predicted crack opening profiles of outer skin at first tearing crack tip: (a) without fatigue closure, and (b) with 0.32 inch fatigue closure (magnification factor = 2.0).

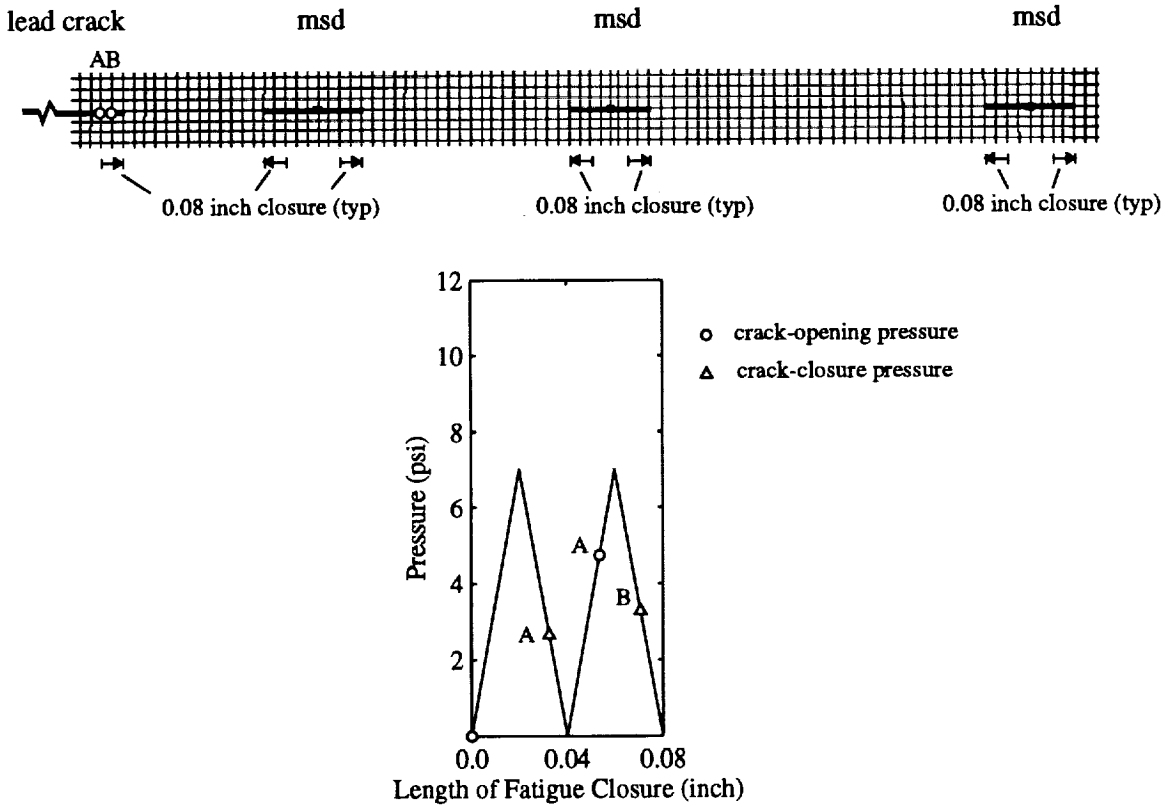

Figure 15: Predicted crack-opening and crack-closure pressure under cyclic loading (cyclic pressure = 7.0 psi, MSD).

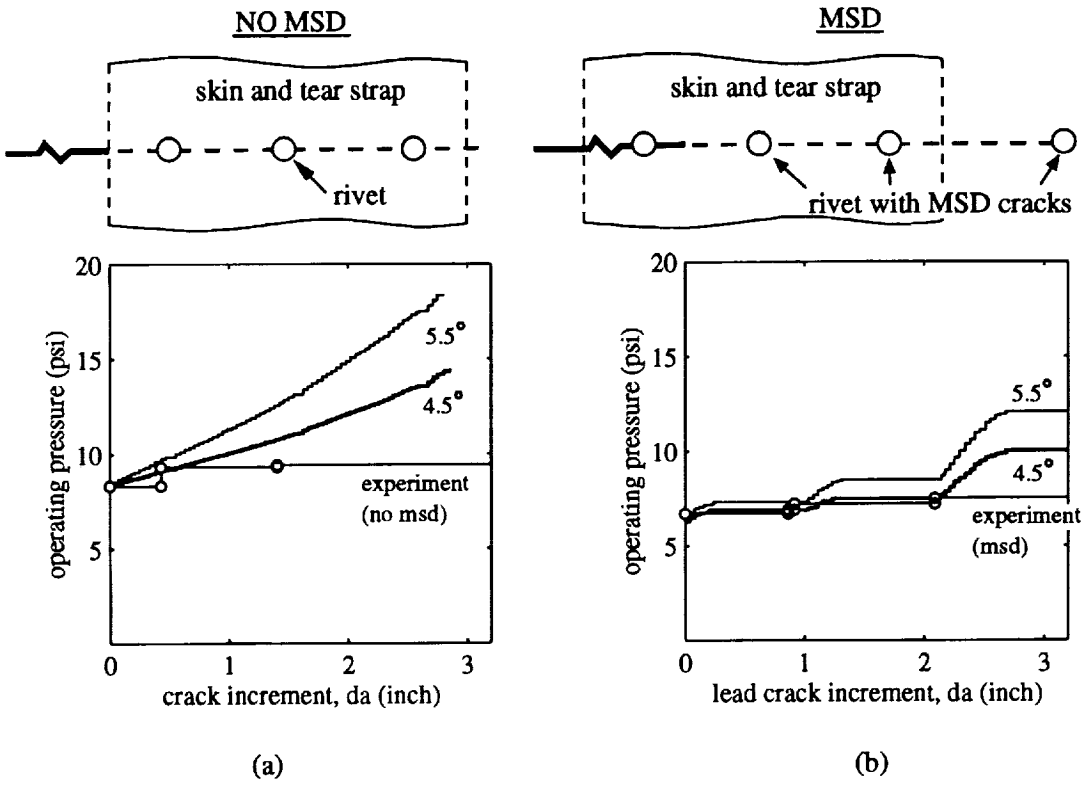

Figure 16: Comparison between predicted crack growth with fatigue closure effects and experimental measurements, (a) without MSD, and (b) with MSD.

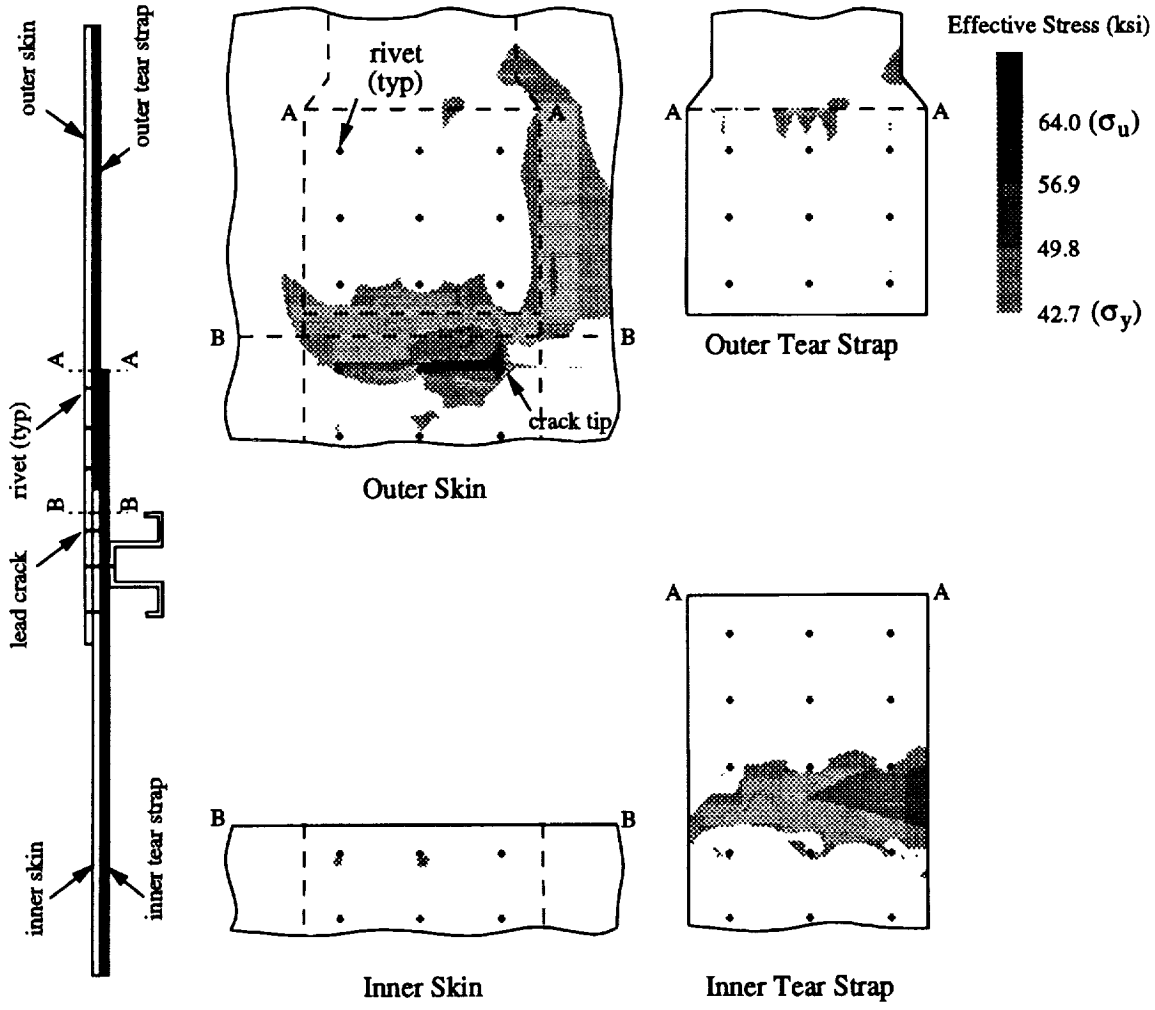

Figure 17: Predicted effective stress distribution (pressure = 9.86 psi, da = 0.5 inch, $CTOA_c$ = 5.5°).

6.2 EFFECTS OF TEAR STRAP FAILURE

A possible cause for the lower residual strengths observed in the test is the occurrence of failure of other structural elements. Figure 17 shows the predicted effective stress distribution in outer skin, inner skin, outer tear strap, and inner tear strap as the crack growth analysis reaches 9.86 psi pressure loading for the case without MSD cracks. Net section yielding is clearly shown in the inner tear strap.

The possible breakage of the inner tear strap during the residual strength test was also reported in [1]. To further investigate this possible MED scenario, a tear strap with rivet holes was modeled. By taking the kinematic boundary conditions from the local fuselage model, a stress concentration around the holes is observed (Figure 18). It is then postulated that the high stress concentration is likely to initiate new cracks from the rivet holes thus leading to breakage of the inner tear strap.

To incorporate the tear strap damage scenario into crack growth analysis, the inner tear strap is cut prior to crack growth analysis as illustrated in Figure 19. The predicted crack-

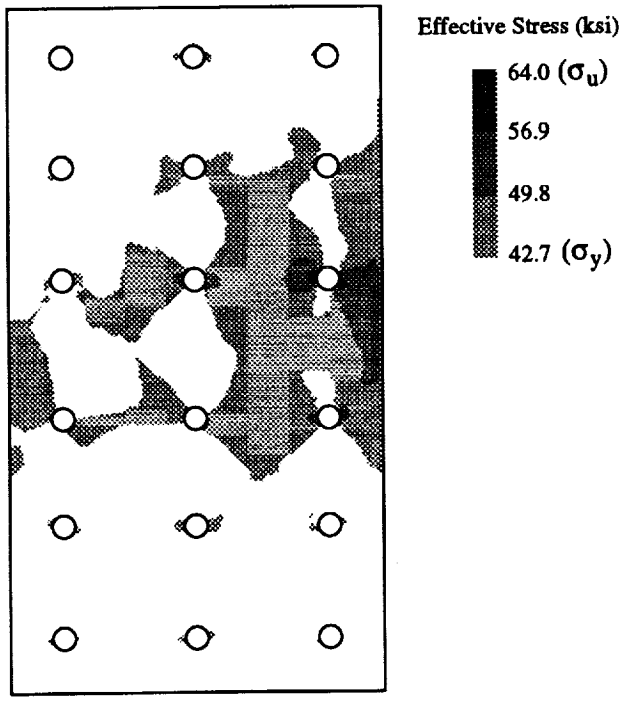

Figure 18: Predicted effective stress distribution of inner tear strap with rivet holes (pressure = 9.86 psi, da = 0.5 inch, $CTOA_c = 5.5°$).

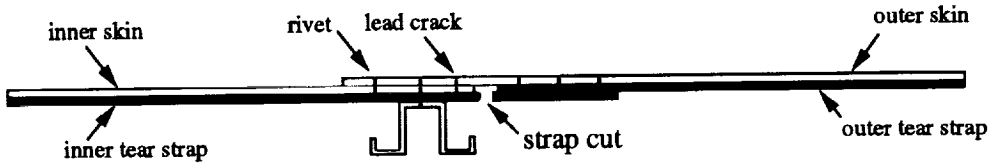

Figure 19: Illustration of broken inner tear strap.

opening pressures of the broken tear strap models with 0.32 and 0.08 inch fatigue closure are 7.0 psi and 3.1 psi for the cases without and with MSD cracks, respectively (*cf*: 7.2 psi and 4.7 psi for the models with the intact tear strap).

Figure 20 shows the predicted crack growth and residual strength for the fuselage models with a broken inner tear strap. The predicted residual strength using 4.5° $CTOA_c$ is within 13% of the experimental observation for the case without MSD cracks and within 1% of the experimental observation for the case with MSD cracks.

The higher predicted residual strength for the case without MSD may be related to the fact that the current model does not faithfully model the crack growth in the vicinity of rivets. In the panel test, the lead crack propagated into and re-initiated from a rivet hole as illustrated in Figure 21. Apparently, neither the CTOA fracture criterion for the lead crack propagation nor the idealized distributed rivet representation have sufficient accuracy in capturing this phenomenon. Further investigation is needed to quantify its effect on residual strength prediction.

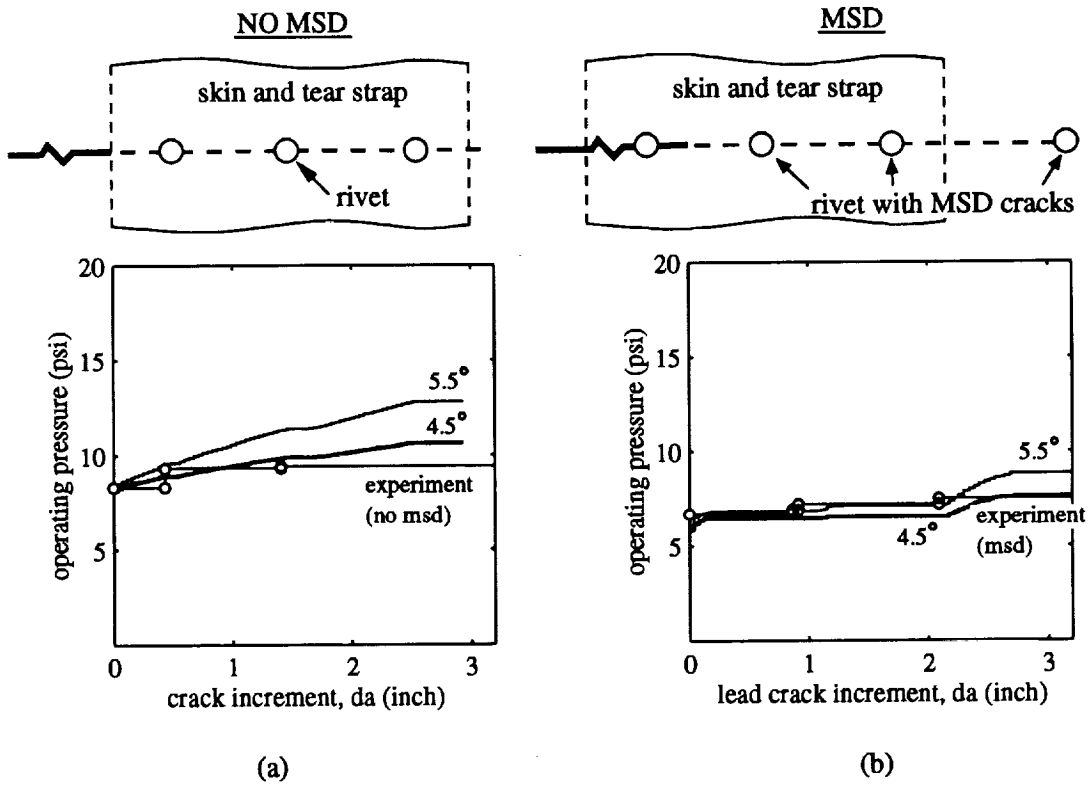

Figure 20: Comparison between predicted crack growth with broken tear strap and experimental measurements, (a) without MSD, and (b) with MSD.

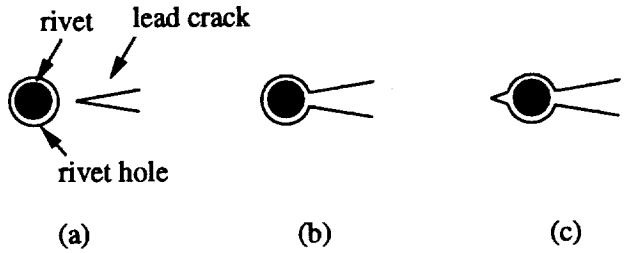

Figure 21: Illustration of crack propagation near rivet: (a) lead crack approaching rivet (b) lead crack growing into rivet hole, and (c) new crack initiating out of rivet hole.

7 CONCLUSIONS

The feasibility and validity of the analysis methodology to predict residual strength of pressurized fuselage structures subjected to MSD are examined. The major findings of this study are:

1. The distributed rivet load treatment of fasteners is crucial for the local crack growth model to accurately predict the stress distribution.

2. The occurrence of small MSD cracks substantially reduces the residual strength of pressurized fuselages. The reduction in residual strength prediction caused by MSD varies from 28% to 47%. A difference of 20% was observed in the tests.

3. The residual strength prediction is sensitive to changes in $CTOA_c$. Altering the $CTOA_c$ from 4.5° to 5.5° changes the predicted residual strength by 17% to 33% for the case without MSD cracks. It changes the predicted residual strength by 12% to 22% for the case with MSD.

4. The residual plastic deformation or the plastic wake from fatigue crack growth has a strong effect on stable crack initiation and a mild effect on residual strength prediction. For crack growth initiation, it is essential to incorporate the plastic wake to accurately predict the starting pressure loading. Neglecting plastic wake effect leads to a totally erroneous prediction of the earlier stable crack growth. For residual strength analysis, the plastic wake increases the predicted residual strength by 3% to 9%.

5. The breakage of the inner tear strap, categorized as possible failure of other structural elements during crack growth, is crucial to residual strength prediction. The occurrence of the broken tear strap reduces the predicted residual strength by 24% to 30%.

The CTOA fracture criterion together with the FRANC3D/STAGS program proves to be an effective tool to simulate: (1) lead crack growth, (2) MSD crack growth, (3) multiple crack interaction, (4) plastic wake from fatigue crack growth, and (5) tear strap failure in pressurized fuselages.

8 ACKNOWLEDGMENTS

The authors would like to thank Dr. James N. Newman, Jr., Dr. David S. Dawicke, Dr. Charles E. Harris, Dr. Charles C. Rankin, Dr. Richard D. Young, Mr. Keith E. Wilkins, Mr. Michael L. Gruber, Dr. Paul Tan, Mr. Richard G. Pettit and Dr. Bruce J. Carter for many helpful discussions. This work was performed with support from the NASA Langley Aircraft Structural Integrity Program under contract NAG-1-1184.

REFERENCES

[1] M. L. Gruber, C. J. Mazur, K. E. Wilkins, and R. E. Worden. Investigation of Fuselage Structure Subject to Widespread Fatigue Damage. Technical Report DOT/FAA/AR-95/47, FAA, February 1996.

[2] M. L. Gruber, K. E. Wilkins, and R. E. Worden. Investigation of Fuselage Structure Subject to Widespread Fatigue Damage. In *Proceedings of the FAA-NASA Symposium on the Continued Airworthiness of Aircraft Structures*, pages 439–460, Atlanta, Georgia, 1996.

[3] D. O. Potyondy, P. A. Wawrzynek, and A. R. Ingraffea. Discrete Crack Growth Analysis Methodology for Through Cracks in Pressurized Fuselage Structures. *International Journal for Numerical Methods in Engineering*, 38:1611–1633, 1995.

[4] C.-S. Chen, P. A. Wawrzynek, and A. R. Ingraffea. Methodology for Fatigue Crack Growth and Residual Strength Prediction with Applications to Aircraft Fuselages. *Computational Mechanics*, 19:527–532, 1997.

[5] C.-S. Chen, P. A. Wawrzynek, and A. R. Ingraffea. Simulation of Stable Tearing and Residual Strength Prediction with Applications to Aircraft Fuselages. In *Proceedings of the FAA-NASA Symposium on Continued Airworthiness of Aircraft Structures*, pages 605–618, 1996.

[6] B. J. Carter, C.-S. Chen, P. A. Wawrzynek, and A. R. Ingraffea. A Topology-Based System for Modeling 3D Crack Growth in Solid and Shell Structures. In *Proceedings of the Ninth International Congress on Fracture, ICF9*, pages 1923–1934, Sydney, Australia, 1997. Elsevior Science Publishers.

[7] J. C. Newman, Jr., D. S. Dawicke, and C. A. Bigelow. Finite-Element Analysis and Fracture SImulation in Thin-Sheet Aluminum Alloy. In *Proceedings of the International Workshop on Structural Integrity of Aging Airplanes*, 1992.

[8] D. S. Dawicke and J. C. Newman, Jr. Residual Strength Predictions for Multiple Site Damage Cracking Using a Three-Dimensional Analysis and a CTOA Criterion. In *Fatigue and Fracture Mechanics: 29th Volume, ASTM STP 1332*, 1998 (in press).

[9] C.-S. Chen, P. A. Wawrzynek, and A. R. Ingraffea. Elastic-Plastic Crack Growth Simulation and Residual Strength Prediction of Thin Plates with Single and Multiple Cracks. In *Fatigue and Fracture Mechanics: 29th Volume, ASTM STP 1332*, 1998 (in press).

[10] J. R. Maclin. Performance of Fuselage Pressure Structure. In *1991 International Conference on Aging Aircraft and Structural Airworthiness*, pages 67–74. NASA Conference Publication 3160, 1991.

[11] M. Miller, K. N. Kaelber, and R. E. Worden. Finite-Element Analysis of Pressure Vessel Panels. In *Proceedings of the International Workshop on Structural Integrity of Aging Airplanes*, 1992.

[12] C. C. Rankin, F. A. Brogan, W. A. Loden, and H. D. Cabiness. *STAGS User Manual Version 2.4*. Lockheed Martin Missiles & Space Co., Inc., Advanced Technology Center, 1997.

[13] C. C. Rankin and F. A. Brogan. *The Computational Structural Mechanics Testbed Structural Element Processor ES5: STAGS Shell Element*, 1991. NASA CR-4358.

[14] T. Swift. Fracture Analysis of Stiffened Structure. In *Damage Tolerance of Metallic Structures: Analysis Methods and Apllication, ASTM STP 842, Philadelphia*, pages 69–107, 1984.

[15] R. D. Young, C. A. Rose, C. G. Dávila, and J. H. Starnes, Jr. Crack Growth and Residual Strength Characteristics of Selected Flat Stiffened Aluminum Panels. Submitted for publication, the first joint DoD/FAA/NASA Conference on Aging Aircraft, Ogden, Utah, July 1997.

[16] R. Singh, J. H. Park, and S. N. Atluri. Growth of Multiple Cracks and Their Linkup in a Fuselage Lap Joint. *AIAA Journal*, 32(11):2260–2268, 1994.

[17] T. Swift. Fracture Analysis of Adhesively Bonded Cracked Panels. *Journal of Engineering Materials and Technology*, 100:10–15, 1978.

[18] J. C. Newman, Jr., D. S. Dawicke, M. A. Sutton, and C. A. Bigelow. A Fracture Criterion For Widespread Cracking in Thin-Sheet Aluminum Alloys. In *International Committee on Aeronautical Fatigue, 17th Symposium, Stockholm, Sweden*, 1993.

[19] D. S. Dawicke, J.C. Newman, Jr., and C. A. Bigelow. Three-Dimensional CTOA and Constraint Effects During Stable Tearing in a Thin-Sheet Material. In *Fracture Mechanics: 26th Volume, ASTM STP 1256, Philadelphia*, pages 223–242, 1995.

[20] C. L. Hom and R. M. McMeeking. Large Crack Tip Opening in Thin Elastic-Plastic Sheets. *International Journal of Fracture*, 45:103–122, 1990.

[21] D. S. Dawicke, J. C. Newman, Jr., M. A. Sutton, and B. E. Amstutz. Influence of Crack History on the Stable Tearing Behavior of a Thin-Sheet Material with Multiple Cracks. In *Proceedings of the FAA-NASA Sixth International Conference on the Continued Airworthiness of Aircraft Structures*, pages 193–212, Atlantic City, New Jersey, 1994.

[22] B.A. Szabó and I. Babuška. *Finite Element Analysis*. John Wiley & Sons, Inc., 1991.

[23] J. C. Newman, Jr. A Finite-Element Analysis of Fatigue Crack Closure. In *Mechanics of Crack Growth, ASTM STP 590, Philadelphia*, pages 281–301, 1976.

[24] W. Elber. Fatigue Crack Closure Under Cyclic Tension. *Engineering Fracture Mechanics*, 2:37–45, 1970.

[25] W. Elber. The Significance of Fatigue Crack Closure. In *Damage Tolerance in Aircraft Structures, ASTM STP 486, Philadelphia*, pages 230–242, 1971.